Schrödinger Dynamics and Berry Phase of Undulatory Locomotion

Alexander E. Cohen [1,2] Alasdair D. Hastewell,[1] Sreeparna Pradhan,[3] Steven W. Flavell,[3] and Jörn Dunkel [1,*]

[1]*Department of Mathematics, Massachusetts Institute of Technology,
77 Massachusetts Avenue, Cambridge, Massachusetts 02139, USA*
[2]*Department of Chemical Engineering, Massachusetts Institute of Technology,
25 Ames Street, Cambridge, Massachusetts 02142, USA*
[3]*Picower Institute for Learning and Memory, Department of Brain and Cognitive Sciences, Massachusetts Institute of Technology,
43 Vassar Street, Cambridge, Massachusetts 02139, USA*

Spectral mode representations play an essential role in various areas of physics, from quantum mechanics to fluid turbulence, but they are not yet extensively used to characterize and describe the behavioral dynamics of living systems. Here, we show that mode-based linear models inferred from experimental live-imaging data can provide an accurate low-dimensional description of undulatory locomotion in worms, centipedes, robots, and snakes. By incorporating physical symmetries and known biological constraints into the dynamical model, we find that the shape dynamics are generically governed by Schrödinger equations in mode space. The eigenstates of the effective biophysical Hamiltonians and their adiabatic variations enable the efficient classification and differentiation of locomotion behaviors in natural, simulated, and robotic organisms using Grassmann distances and Berry phases. While our analysis focuses on a widely studied class of biophysical locomotion phenomena, the underlying approach generalizes to other physical or living systems that permit a mode representation subject to geometric shape constraints.

Undulatory propulsion is the natural locomotion strategy [1,2] of many aquatic and terrestrial animals, from worms [3–7] and fish [8,9] to lizards [10,11] and snakes [12,13]. The mechanical wave patterns that drive undulatory motion reflect an animal's behavioral state [14], providing a macroscopic physical readout of the underlying biochemical and neuronal excitations. Recent advances in automated live imaging [15,16] enable simultaneous observations of macroscopic locomotion dynamics and microscopic cellular activity [17–22], producing rapidly growing multiscale datasets [23] that have to be tracked [24–26] and translated into predictive and interpretable models. Despite recent major progress in the experimental characterization [17–21] and biophysical description of specific organisms [4,10,27–34], a quantitative model inference framework for comparing experimentally observed undulatory dynamics within and across species has yet to be developed. In addition to providing unifying biophysical insights spanning different animal kingdoms, such a framework would also allow for a direct comparison of living systems with computational models [35,36] and biomimetic robotic devices [37,38].

Here, we use spectral mode representations to identify symmetry-constrained dynamical models that can capture and distinguish the undulatory locomotion of worms (*Caenorhabditis elegans*) [14], neuromechanical worm models [35], Mojave shovel-nosed snakes (*Chionactis*

occipitalis) [39], mechanical snakes, and centipedes (*Lithobius forficatus*). Compared with traditional continuum descriptions of undulatory shape deformations in position space, formulating locomotion models in mode space [40–43] offers several theoretical and practical advantages: (i) high-dimensional experimental data can be efficiently compressed to obtain an interpretable low-dimensional representation; (ii) the mode dynamics reduces to a system of linear ordinary differential equations (ODEs); (iii) physical symmetries and biological constraints can be efficiently encoded through the structure of the dynamical matrix; (iv) all model parameters can be directly inferred from experimental data using ODE sensitivity methods [44,45] that exploit the imposed matrix structure [46]. In particular, for undulatory locomotion, we find that translational invariance, rotational invariance, and length constraints generically lead to a Schrödinger equation [47] in mode space. Similar to the characterization of quantum systems in terms of their spectra and eigenstates [48], the eigenspaces of the effective Hamiltonians enable an efficient classification of the locomotion dynamics of worms, snakes, robots, and computational models. Furthermore, transitions between animal behavioral states are encoded in the time evolution of the Hamiltonian and thus can be detected using Berry phases [49]. While our discussion focuses on an important subclass of biophysical dynamics, the underlying approach generalizes to other
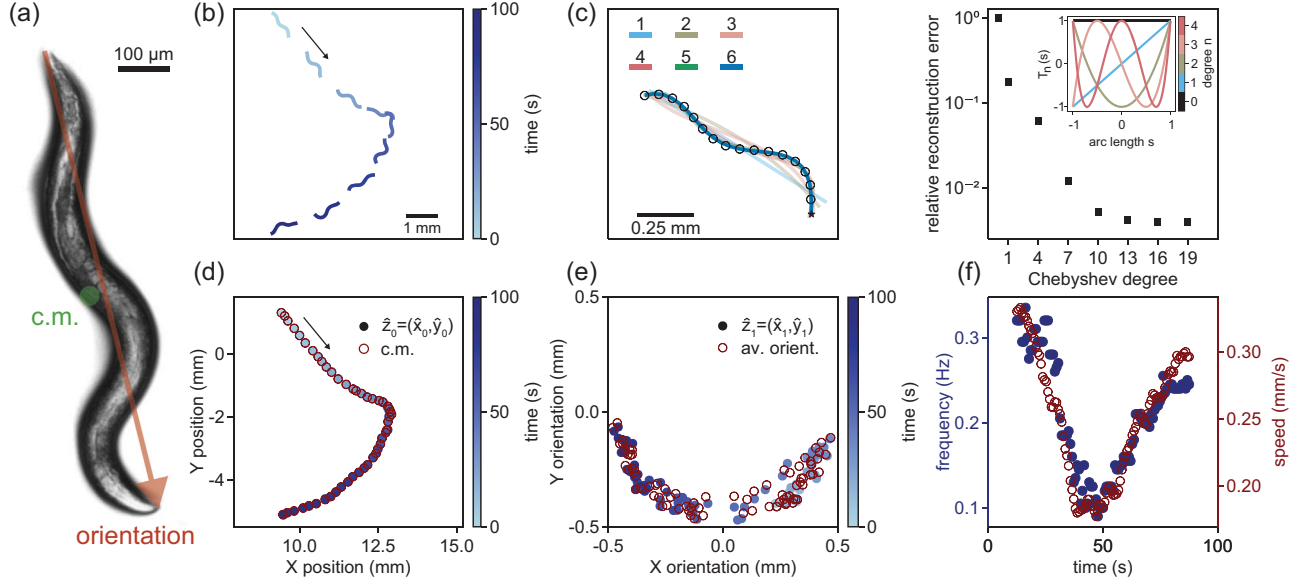
FIG. 1. Chebyshev mode representation enables an efficient and interpretable low-dimensional description of undulatory locomotion across species and model systems. (a) Experimental image of *C. elegans* worm with center of mass (c.m.) and mean orientation overlayed. (b) Tracked centerline of worm over 100 s. Arrow indicates direction of motion. (c) A small number of Chebyshev polynomials suffices to accurately reconstruct the worm shape (left). Faint colored lines correspond to centerline reconstructions at different polynomial degrees. Reconstruction error (right) decays rapidly as the Chebyshev degree n increases. (d) The zeroth-order Chebyshev coefficients follow closely the worm's geometric c.m., illustrating the physical interpretability of the Chebyshev mode representation. (e) Similarly, the first-order Chebyshev coefficients represent the tail-to-head worm orientation. (f) The mode-averaged dominant frequency of Chebyshev mode oscillations correlates closely with the locomotion speed of the worm.

physical or living systems that permit a mode representation while being subject to exact or approximate geometric constraints.

The planar undulatory locomotion of an elongated wormlike object can be described by its centerline position in the complex plane $z(s,t) = x(s,t) + iy(s,t)$, where $s \in [-1, 1]$ is the arc length and t denotes time [Figs. 1(a) and 1(b)]. While tens to hundreds of points are typically required for an accurate depiction of an organism's shape in position space [17], interpretable lower-dimensional representations can often be obtained by projecting on suitable polynomial, trigonometric, or other basis functions [27,50]. Although system-dependent representations, such as principal-component-analysis-based eigenworms [27,32], yield near-optimal compression for a specific organism under fixed experimental conditions, system-independent orthogonal basis expansions enable direct comparisons across different systems and experimental conditions (see Supplemental Material [51]). Moreover, system-dependent representations are often nondifferentiable, making physically constrained modeling analytically intractable. Here, we use Chebyshev polynomials [52] of the first kind $T_k(s)$, which are known to have advantageous analytical and computational properties; in principle, other basis functions could be chosen as well. The dynamics of the complex scalar field $z(s,t) = x(s,t) + iy(s,t)$ can then be represented in terms of its leading Chebyshev

coefficients $\hat{z}_k(t) = \hat{x}_k(t) + i\hat{y}_k(t)$ up to degree n, defined by

$$z(s,t) = \sum_{k=0}^{n} T_k(s)\hat{z}_k(t). \quad (1)$$

For the experimental imaging data analyzed below, $n+1 = 10$ modes suffice for achieving reconstruction errors less than 1% [Fig. 1(c) and [51]]. Since Chebyshev polynomials are orthogonal with respect to the weight function $w(s) = 1/\sqrt{1-s^2}$ [52], the coefficients $\hat{z}_k$ are obtained by taking inner products,

$$\hat{z}_k(t) = \frac{\gamma_k}{\pi} \int_{-1}^{1} ds\, w(s)\, T_k(s)\, z(s,t), \quad (2)$$

where $\gamma_0 = 1$ and $\gamma_k = 2$ for $k > 0$. We illustrate the physical meaning of the Chebyshev modes using recent tracking microscopy video data [17] for *C. elegans* [Figs. 1(a) and 1(b)], a widely studied model organism with 95 body wall muscle cells, 302 neurons, and a rich set of behavioral states and corresponding locomotion patterns [14]. The real and imaginary parts of $\hat{z}_0(t) = \hat{x}_0(t) + i\hat{y}_0(t)$, obtained from Eq. (2) with $T_0(s) = 1$, describe the w-weighted Chebyshev c.m. of the moving worm, which follows closely the geometric c.m. [Fig. 1(d)]. The degree-1 coefficient $\hat{z}_1(t)$ with $T_1(s) = s$ represents the mean

orientation of the worm [Fig. 1(e) and [51]]. Similarly, the Chebyshev coefficients $\hat{z}_k$ of degree $k \geq 2$ encode curvature and higher deformation modes [Fig. 1(c), inset]. The average dominant frequency across the mode oscillations closely matches the speed of the worm in real space [Fig. 1(f) and [51]].

Equipped with this representation, we seek to formulate a dynamical model for undulatory motion in mode space. Defining a combined mode vector $\boldsymbol{\Psi}(t) = [\hat{z}_0, \ldots, \hat{z}_n] \in \mathbb{C}^{n+1}$, the most general coupled linear first-order dynamics is $\dot{\boldsymbol{\Psi}} = M\boldsymbol{\Psi}$. Note that the complex formulation is manifestly rotationally invariant, since a rotation by θ corresponds to multiplication by $e^{i\theta}$. Incorporating additional symmetries and invariances into the model imposes further structure on M. Translational invariance requires the Chebyshev c.m. $\boldsymbol{\psi}_0 = \hat{z}_0$ to decouple from the higher degree coefficients $\hat{\boldsymbol{\psi}} = [\hat{z}_1, \ldots, \hat{z}_n] \in \mathbb{C}^n$ that describe the orientation and shape [51]. Abbreviating $\partial_s z = \partial z/\partial s$, an additional biophysical constraint for undulatory motion is that the length of the centerline $\ell(t) = \int_{-1}^{1} ds |\partial_s z|$ remains approximately constant (see Supplemental Material [51]). In mode space, length variations can be bounded by conserving the convex quadratic functional

$$\tilde{\ell}^2 = \int_{-1}^{1} ds |\partial_s z|^2 = \hat{\boldsymbol{\psi}}^\dagger W \hat{\boldsymbol{\psi}}, \tag{3}$$

where W is a symmetric matrix with elements $W_{k,m} = \int_{-1}^{1} ds \partial_s T_k(s) \partial_s T_m(s)$. In particular, W is positive definite and can thus be interpreted as a basis-specific metric. Taylor expanding the curve length ℓ around the space and time average of $|\partial_s z|^2$, denoted by $\langle \cdot \rangle$, shows that ℓ is approximately proportional to $\tilde{\ell}^2/\sqrt{\langle |\partial_s z|^2 \rangle}$; additionally,

the Cauchy-Schwarz inequality implies $\ell^2 \leq 2\tilde{\ell}^2$ [51]. Therefore, demanding constant $\tilde{\ell}$ corresponds to an energetic penalty against contracting or lengthening and ensures ℓ remains approximately constant and bounded. Keeping Eq. (3) constant forces the shape modes $\hat{\boldsymbol{\psi}}$ onto a hyperellipsoid, with axes determined by W. Using the Cholesky factorization $W = LL^\dagger$, this hyperellipsoid can be transformed to a unit hypersphere by defining the rescaled mode vector $\boldsymbol{\psi} = (L^\dagger/\tilde{\ell})\hat{\boldsymbol{\psi}}$. Under this transformation, the length constraint (3) becomes a normalization condition

$$\boldsymbol{\psi}^\dagger \boldsymbol{\psi} = 1. \tag{4a}$$

Combined with rotational and translational invariance, the normalization restricts the class of permissible linear models to the form [51]

$$\dot{\boldsymbol{\psi}}_0 = \boldsymbol{h}_0^\dagger \boldsymbol{\psi}, \tag{4b}$$

$$i\dot{\boldsymbol{\psi}} = H\boldsymbol{\psi}, \tag{4c}$$

where $\boldsymbol{h}_0$ is a complex vector and H is a complex Hermitian matrix with real eigenvalues. Equation (4b) describes how the Chebyshev c.m. dynamics couples to the body oscillations through $\boldsymbol{h}_0$. Equation (4c), which governs the shape dynamics, is mathematically equivalent to a Schrödinger equation with Hamiltonian H [47].

To confirm that Eqs. (4) can indeed describe and distinguish the undulatory dynamics of *C. elegans* worms [17] and other organisms and systems, we implemented an inference framework (see Supplemental Material [51]) for estimating the propulsion vector $\boldsymbol{h}_0(t)$ and the shape Hamiltonian $H(t)$ from experimental data for short straight-motion segments (Figs. 2 and 3), as well as longer
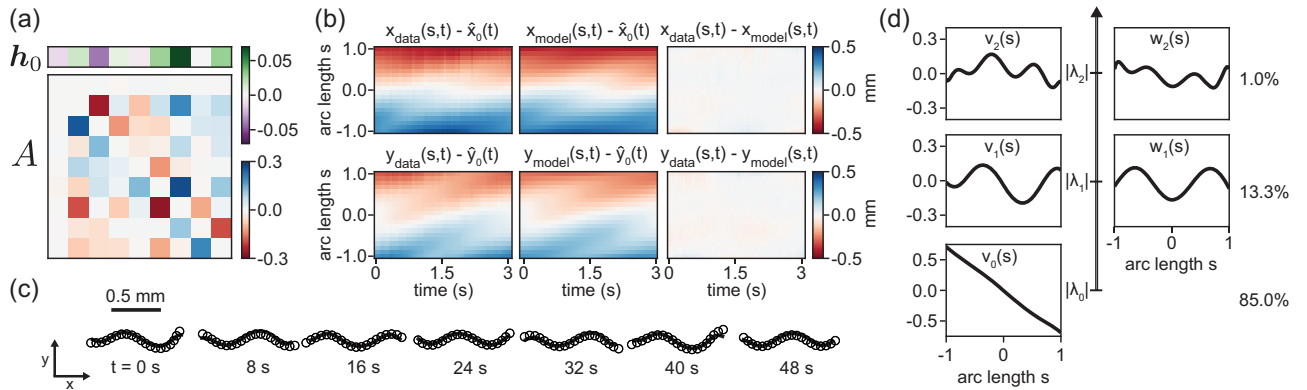

FIG. 2. Inferred Schrödinger dynamics replicate stereotypical *C. elegans* locomotion. (a) Representative real propulsion vector $\boldsymbol{h}_0$ and Hamiltonian $H = S + iA$ for a minimal periodic straight-motion model [Eq. (4) with $S = 0$ and equidistant spectrum of H] fitted to data from a single oscillation period ($\tau = 3.05$ s). (b) Kymographs of $x(s, t)$ and $y(s, t)$ coordinate fields for observed data (left) and model prediction (middle) show little deviation (right), confirming that Eq. (4) can accurately capture undulatory shape dynamics of *C. elegans*. (c) Real-space dynamics predicted by the Schrödinger model (line) is consistent with the observed worm dynamics (circles); see Supplemental Material, Video S1 [51]. Experimental data have been periodically extended for visualization to avoid overlapping body segments. (d) Real-space shape functions [Eq. (5)] corresponding to the three smallest magnitude eigenvalues, $\lambda_k^\pm = \pm k\lambda$ for $k = 0, 1, 2$, account for $> 98\%$ of the shape dynamics, enabling a generalizable low-rank description. More complex turning dynamics can be described using time-varying Hamiltonians with unconstrained spectra (Fig. 4 and [51]).

trajectories that include turning events (Fig. 4). Before outlining the model inference procedure, recall that any Hermitian matrix H can be decomposed in the form $H = S + iA$, where S is real symmetric and A real skew symmetric. In the present context, S encodes turning behavior, whereas A governs straight locomotion: For straight motions, x and y modes do not couple significantly, so that h_0 is real and $S \approx 0$ and, hence, $H \approx iA$ in this case [Fig. 4(a) and [51]].

Generally, both h_0 and H can be efficiently determined from tracked centerlines via a physics-informed dynamic mode decomposition [53,54] that exploits matrix structure [46]. Since H is Hermitian, it permits the decomposition $H = U\Lambda U^\dagger$, where U is unitary and Λ is a real diagonal matrix. This leaves n^2 parameters in U and Λ plus $2n$ in h_0 to be estimated from data. If available data are limited, the number of parameters can be reduced further by imposing additional constraints on the spectrum of H (see Supplemental Material [51]). To avoid numerical differentiation of noisy data, our inference scheme compares numerically integrated predictions from Eqs. (4) directly to the experimental data [51]. Our algorithm sequentially optimizes U, Λ, and h_0 by minimizing deviations from both real-space body shapes and mode-space trajectories, to balance shape matching with model generalizability and to prevent overfitting [51]. Minimization is performed using gradient-based optimization [55–57] with forward mode automatic differentiation through the ODE solver [43–45].

This scheme makes it possible to infer the instantaneous shape Hamiltonians $H(t)$ and the propulsion vectors $h_0(t)$ from just a single oscillation period for straight motions (Figs. 2 and 3), as well as from longer curved trajectories (Fig. 4). For *C. elegans* (Fig. 2), as well as for previously proposed neuromechanical worm models [35], *C. occipitalis* snakes [39], snake robots, and *L. forficatus* centipedes (Fig. 3), the best-fit straight-motion models based on Eqs. (4) with $H = iA$ accurately capture the undulatory dynamics ([51], Video S1).

Since the shape dynamics are encoded by the Hamiltonian H, we can use its eigenstates to compare and classify undulatory motion across species and systems [48]. Indeed, for straight motions, it suffices to study the eigenstates of A. Considering $n = 9$ as before, A has one zero eigenvalue $\lambda_0 = 0$ corresponding to the zero-mode eigenvector ϕ_0, and four distinct pairs of opposite sign eigenvalues $\lambda_{k\geq 1}^\pm$ with complex conjugate eigenvectors $\phi_k^\pm$, where $\phi_k^+ = (\phi_k^-)^*$. We define two real orthogonal mode-space vectors $v_k = \mathrm{Re}(\phi_k^+)$ and $w_k = \mathrm{Im}(\phi_k^+)$ that span the eigenspace of $\phi_k^\pm$. The real-space shape functions corresponding to the real mode-space vectors are

$$v_k(s) = \ell[L^{-1}\mathbf{T}(s)]^\dagger v_k, \qquad w_k(s) = \ell[L^{-1}\mathbf{T}(s)]^\dagger w_k, \quad (5)$$

where $\mathbf{T}(s) = [T_1(s), T_2(s), ..., T_n(s)]$ is a vector of Chebyshev functions. Time-varying linear combinations
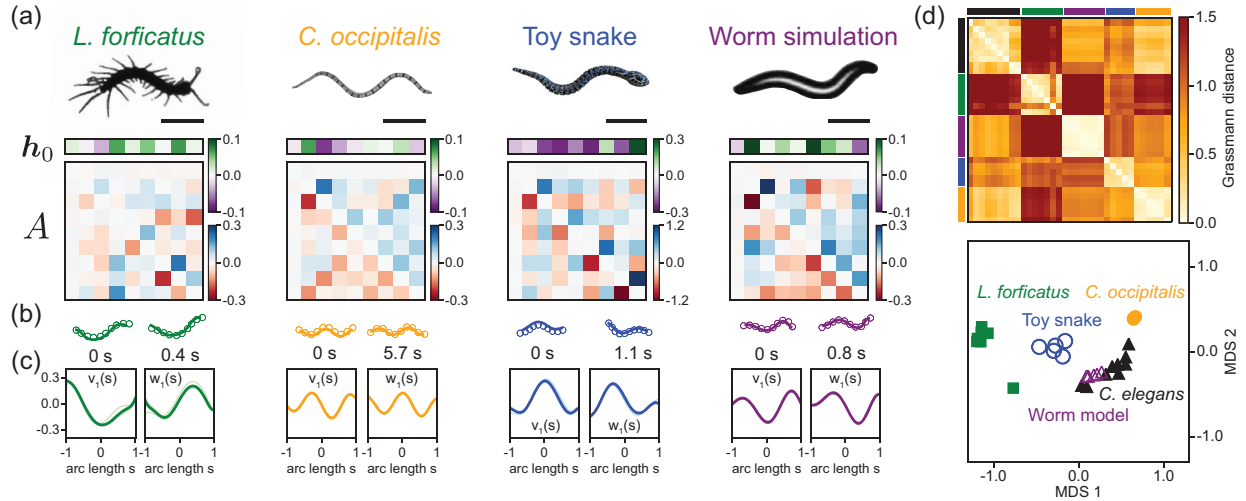

FIG. 3. Mode-space Hamiltonians provide a compact dynamical description of undulatory motion across different species and model systems. (a) Living and nonliving systems [35,39] analyzed here and representative straight-motion Hamiltonians $H = iA$ inferred from a single oscillation period. The eigenspaces of the Hamiltonians enable the comparison and classification of undulation dynamics in (d). Scale bars are 8 mm (centipede), 10 cm (snake), 10 cm (toy snake), 0.25 mm (worm model). (b) Inferred Schrödinger model dynamics (line) provide an accurate description of the observed dynamics (circles). Models were fitted on a single period $\tau = 0.19$ s (centipede), 0.33 s (snake), 0.45 s (toy snake), 2.2 s (worm model); see also [51], Video S1. Experimental data have been periodically extended for visualization to avoid overlapping body segments. (c) The dominant shape eigenvectors $v_1(s)$ and $w_1(s)$ are consistent within each species and capture differences between species. (d) Pairwise Grassmann distances between subspaces spanned by first excited eigenstates of the Hamiltonians (top) and its 2D planar embedding [bottom, constructed by a multidimensional scaling (MDS)] capture the similarities and differences between undulatory locomotion in organisms, model simulations, and robots. Each point corresponds to a different trajectory.

of $v_k(s)$ and $w_k(s)$ give the instantaneous centerline reconstruction [51]. We find that the zero state $v_0(s)$ is close to the best-fit straight line through the motion, accounting for 85% of the time-averaged centerline reconstruction, while most of the oscillations are accounted for by the first excited states $v_1(s)$ and $w_1(s)$ corresponding to the smallest magnitude nonzero eigenvalues (13.3%). Since most ($> 98\%$) of the dynamics is captured by the zero state and first excited states, one can, in fact, further reduce the complexity of the Schrödinger model, by approximating A through its projection $\hat{A}$ on the eigenspaces corresponding to the first two distinct eigenvalues. This additional low-rank approximation also further reduces the risk of overfitting and hence improves model generalizability, similar to sparsity promotion in other dynamical inference methods [58].

The compact low-rank characterization of the undulatory shape dynamics makes it possible to compare the locomotion behaviors of *C. elegans*, previously proposed neuromechanical worm models [35], *C. occipitalis* snakes [39], robotic toy snakes, and centipedes, by measuring the Grassmann distance [59] between the dominant eigenspaces of $\hat{A}$. As most of the variation of the oscillatory dynamics is contained in the first excited states v_1 and w_1, we determined the pairwise Grassmann distances between the eigenspaces spanned by v_1 and w_1 for the various systems (see Supplemental Material [51]). Both the distance matrix and a corresponding 2D phase diagram constructed by multidimensional scaling reveal that the neuromechanical worm model [35] succeeds in reproducing key dynamical aspects of *C. elegans* locomotion, whereas the robotic toy snake used in our experiments is equally far from real snake or worm locomotion [Fig. 3(d)].

Beyond interspecies comparisons, the above framework enables us to characterize behavioral transitions by borrowing concepts from quantum mechanics, such as Berry phases and adiabatic approximations [49]. To illustrate this, we focus on a longer *C. elegans* trajectory during which the worm performs a turn [Fig. 4(a)] after briefly reversing its motion due to a change in neuromechanical activity [60]. By reconstructing the time-dependent Hamiltonian $H(t) = S(t) + iA(t)$ along the path [51], we observe a significant increase in $\|S(t)\|$ at the turn, whereas $A(t)$ remains approximately constant throughout. When the worm switches on S to facilitate a turn, the instantaneous eigenvectors of $H(t)$ change [51], signaled by a rapid change of the Berry phase [blue curve in Fig. 4(b)]. Furthermore, while the locomotion dynamics before the turn is well described by an adiabatic approximation (see Supplemental Material [51], Video S2), this approximation becomes inaccurate during the turn [red curve in Fig. 4(b)].

From a practical perspective, the above results show how symmetry-constrained mode representations can facilitate a low-dimensional description and efficient classification of biophysical dynamics. The underlying inference framework is directly applicable to diagnose and quantify
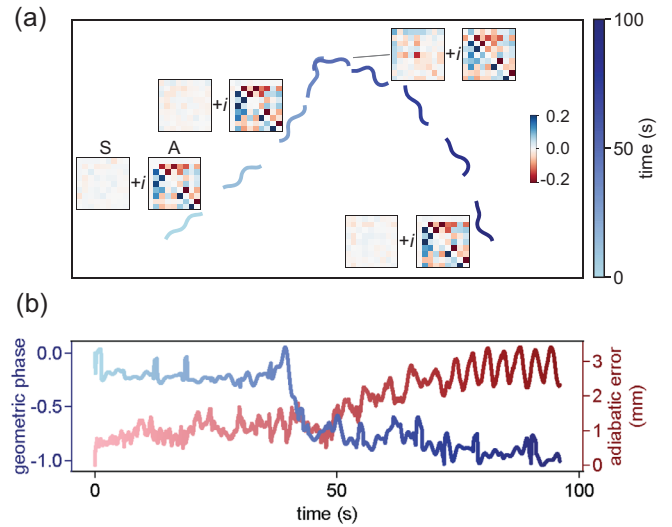

FIG. 4. Breakdown of adiabaticity during reversal turning behavior of *C. elegans*. (a) The turning part $S(t)$ of the Hamiltonian $H(t) = S(t) + iA(t)$ becomes switched on at the turn. (b) The turn is signaled by a sudden change in the geometric Berry phase (blue) of the dominant eigenvector [51], and the rms reconstruction error of the adiabatic approximation increases noticeably after the turn (see Supplemental Material [51], Video S2).

the effects of genetic or chemical perturbations on animal locomotion within and across species. From a theoretical perspective, the fact that translational and rotational invariance combined with a quadratic integral constraint generically lead to a Schrödinger equation [47] in mode space promises advances in the quantitative understanding of biological systems, as the comprehensive toolbox of quantum physics [61,62] now becomes available to characterize and predict behavioral dynamics.

*dunkel@mit.edu

[1] J. Gray, Undulatory propulsion, J. Cell Sci. **3**, 551 (1953).
[2] N. Cohen and J. H. Boyle, Swimming at low Reynolds number: A beginners guide to undulatory locomotion, Contemp. Phys. **51**, 103 (2010).

[3] E. Niebur and P. Erdös, Theory of the locomotion of nematodes: Dynamics of undulatory progression on a surface, Biophys. J. **60**, 1132 (1991).

[4] T. Majmudar, E. E. Keaveny, J. Zhang, and M. J. Shelley, Experiments and theory of undulatory locomotion in a simple structured medium, J. R. Soc. Interface **9**, 1809 (2012).

[5] A. Kudrolli and B. Ramirez, Burrowing dynamics of aquatic worms in soft sediments, Proc. Natl. Acad. Sci. U.S.A. **116**, 25569 (2019).

[6] J. Sznitman, P. K. Purohit, P. Krajacic, T. Lamitina, and P. E. Arratia, Material properties of Caenorhabditis elegans swimming at low Reynolds number, Biophys. J. **98**, 617 (2010).

[7] X. N. Shen and P. E. Arratia, Undulatory Swimming in Viscoelastic Fluids, Phys. Rev. Lett. **106**, 208101 (2011).

[8] A. J. Smits, Undulatory and oscillatory swimming, J. Fluid Mech. **874**, P1 (2019).

[9] J. G. Thewissen and F. Fish, Locomotor evolution in the earliest cetaceans: Functional model, modern analogues, and paleontological evidence, Paleobiology **23**, 482 (1997).

[10] R. D. Maladen, Y. Ding, P. B. Umbanhowar, A. Kamor, and D. I. Goldman, Mechanical models of sandfish locomotion reveal principles of high performance subsurface sandswimming, J. R. Soc. Interface **8**, 1332 (2011).

[11] B. Chong, T. Wang, E. Erickson, P. J. Bergmann, and D. I. Goldman, Coordinating tiny limbs and long bodies: Geometric mechanics of lizard terrestrial swimming, Proc. Natl. Acad. Sci. U.S.A. **119**, e2118456119 (2022).

[12] Z. Guo and L. Mahadevan, Limbless undulatory propulsion on land, Proc. Natl. Acad. Sci. U.S.A. **105**, 3179 (2008).

[13] D. L. Hu, J. Nirody, T. Scott, and M. J. Shelley, The mechanics of slithering locomotion, Proc. Natl. Acad. Sci. U.S.A. **106**, 10081 (2009).

[14] S. W. Flavell, D. M. Raizen, and Y.-J. You, Behavioral states, Genetics **216**, 315 (2020).

[15] W. Hong, A. Kennedy, X. P. Burgos-Artizzu, M. Zelikowsky, S. G. Navonne, P. Perona, and D. J. Anderson, Automated measurement of mouse social behaviors using depth sensing, video tracking, and machine learning, Proc. Natl. Acad. Sci. U.S.A. **112**, E5351 (2015).

[16] N. Pokala and S. W. Flavell, *Recording and quantifying C. elegans behavior, in C. elegans* (Springer, New York, 2022), pp. 357–373, 10.1007/978-1-0716-2181-3_20.

[17] N. Cermak, K. Y. Stephanie, R. Clark, Y.-C. Huang, S. N. Baskoylu, and S. W. Flavell, Whole-organism behavioral profiling reveals a role for dopamine in state-dependent motor program coupling in C. elegans, eLife **9**, e57093 (2020).

[18] F. B. Shipley, C. M. Clark, M. J. Alkema, and A. M. Leifer, Simultaneous optogenetic manipulation and calcium imaging in freely moving C. elegans, Front. Neural Circuits **8**, 28 (2014).

[19] A. M. Leifer, C. Fang-Yen, M. Gershow, M. J. Alkema, and A. D. Samuel, Optogenetic manipulation of neural activity in freely moving Caenorhabditis elegans, Nat. Methods **8**, 147 (2011).

[20] R. Prevedel, Y.-G. Yoon, M. Hoffmann, N. Pak, G. Wetzstein, S. Kato, T. Schrödel, R. Raskar, M. Zimmer, E. S. Boyden *et al.*, Simultaneous whole-animal 3D imaging of neuronal activity using light-field microscopy, Nat. Methods **11**, 727 (2014).

[21] K. Bozek, L. Hebert, Y. Portugal, A. S. Mikheyev, and G. J. Stephens, Markerless tracking of an entire honey bee colony, Nat. Commun. **12**, 1733 (2021).

[22] M. Liu, A. K. Sharma, J. W. Shaevitz, and A. M. Leifer, Temporal processing and context dependency in Caenorhabditis elegans response to mechanosensation, eLife **7**, e36419 (2018).

[23] L. Hebert, T. Ahamed, A. C. Costa, L. O'Shaughnessy, and G. J. Stephens, Wormpose: Image synthesis and convolutional networks for pose estimation in C. elegans, PLoS Comput. Biol. **17**, e1008914 (2021).

[24] M. W. Mathis and A. Mathis, Deep learning tools for the measurement of animal behavior in neuroscience, Curr. Opin. Neurobiol. **60**, 1 (2020).

[25] T. D. Pereira, D. E. Aldarondo, L. Willmore, M. Kislin, S. S.-H. Wang, M. Murthy, and J. W. Shaevitz, Fast animal pose estimation using deep neural networks, Nat. Methods **16**, 117 (2019).

[26] A. Mathis, P. Mamidanna, K. M. Cury, T. Abe, V. N. Murthy, M. W. Mathis, and M. Bethge, Deeplabcut: Markerless pose estimation of user-defined body parts with deep learning, Nat. Neurosci. **21**, 1281 (2018).

[27] G. J. Stephens, B. Johnson-Kerner, W. Bialek, and W. S. Ryu, Dimensionality and dynamics in the behavior of C. elegans, PLoS Comput. Biol. **4**, e1000028 (2008).

[28] A. C. Costa, T. Ahamed, and G. J. Stephens, Adaptive, locally linear models of complex dynamics, Proc. Natl. Acad. Sci. U.S.A. **116**, 1501 (2019).

[29] T. Ahamed, A. C. Costa, and G. J. Stephens, Capturing the continuous complexity of behaviour in Caenorhabditis elegans, Nat. Phys. **17**, 275 (2021).

[30] A. Hosoi and D. I. Goldman, Beneath our feet: Strategies for locomotion in granular media, Annu. Rev. Fluid Mech. **47**, 431 (2015).

[31] Y. Ozkan-Aydin, D. I. Goldman, and M. S. Bhamla, Collective dynamics in entangled worm and robot blobs, Proc. Natl. Acad. Sci. U.S.A. **118**, e2010542118 (2021).

[32] G. J. Berman, D. M. Choi, W. Bialek, and J. W. Shaevitz, Mapping the stereotyped behaviour of freely moving fruit flies, J. R. Soc. Interface **11**, 20140672 (2014).

[33] E. Lauga and T. R. Powers, The hydrodynamics of swimming microorganisms, Rep. Prog. Phys. **72**, 096601 (2009).

[34] H. C. Astley, J. R. Mendelson III, J. Dai, C. Gong, B. Chong, J. M. Rieser, P. E. Schiebel, S. S. Sharpe, R. L. Hatton, H. Choset *et al.*, Surprising simplicities and syntheses in limbless self-propulsion in sand, J. Exp. Biol. **223**, jeb103564 (2020).

[35] J. H. Boyle, S. Berri, and N. Cohen, Gait modulation in C. elegans: An integrated neuromechanical model, Front. Comput. Neurosci. **6**, 10 (2012).

[36] G. P. Sarma, C. W. Lee, T. Portegys, V. Ghayoomie, T. Jacobs, B. Alicea, M. Cantarelli, M. Currie, R. C. Gerkin, S. Gingell *et al.*, Openworm: Overview and recent advances in integrative biological simulation of Caenorhabditis elegans, Phil. Trans. R. Soc. B **373**, 20170382 (2018).

[37] H. Marvi, C. Gong, N. Gravish, H. Astley, M. Travers, R. L. Hatton, J. R. Mendelson III, H. Choset, D. L. Hu, and

D. I. Goldman, Sidewinding with minimal slip: Snake and robot ascent of sandy slopes, Science **346**, 224 (2014).

[38] J. Aguilar, T. Zhang, F. Qian, M. Kingsbury, B. McInroe, N. Mazouchova, C. Li, R. Maladen, C. Gong, M. Travers *et al.*, A review on locomotion robophysics: The study of movement at the intersection of robotics, soft matter and dynamical systems, Rep. Prog. Phys. **79**, 110001 (2016).

[39] P. E. Schiebel, J. M. Rieser, A. M. Hubbard, L. Chen, D. Z. Rocklin, and D. I. Goldman, Mechanical diffraction reveals the role of passive dynamics in a slithering snake, Proc. Natl. Acad. Sci. U.S.A. **116**, 4798 (2019).

[40] A. Goldschmidt, E. Kaiser, J. L. Dubois, S. L. Brunton, and J. N. Kutz, Bilinear dynamic mode decomposition for quantum control, New J. Phys. **23**, 033035 (2021).

[41] P. J. Schmid, Dynamic mode decomposition of numerical and experimental data, J. Fluid Mech. **656**, 5 (2010).

[42] J. H. Tu, C. W. Rowley, D. M. Luchtenburg, S. L. Brunton, and J. N. Kutz, On dynamic mode decomposition: Theory and applications, J. Comp. Nonlin. Dyn. **1**, 391 (2014).

[43] N. Romeo, A. Hastewell, A. Mietke, and J. Dunkel, Learning developmental mode dynamics from single-cell trajectories, eLife **10**, e68679 (2021).

[44] Y. Ma, V. Dixit, M. J. Innes, X. Guo, and C. Rackauckas, A comparison of automatic differentiation and continuous sensitivity analysis for derivatives of differential equation solutions, in *Proceedings of the 2021 IEEE High Performance Extreme Computing Conference (HPEC)* (IEEE, New York, 2021), pp. 1–9, 10.1109/HPEC49654.2021 .9622796.

[45] C. Rackauckas, Y. Ma, J. Martensen, C. Warner, K. Zubov, R. Supekar, D. Skinner, A. Ramadhan, and A. Edelman, Universal differential equations for scientific machine learning, arXiv:2001.04385.

[46] L. Sorber, M. Van Barel, and L. De Lathauwer, Structured data fusion, IEEE J. Sel. Top. Signal Process. **9**, 586 (2015).

[47] E. Schrödinger, An undulatory theory of the mechanics of atoms and molecules, Phys. Rev. **28**, 1049 (1926).

[48] D. J. Griffiths and D. F. Schroeter, *Introduction to Quantum Mechanics* (Cambridge University Press, Cambridge, 2018).

[49] M. V. Berry, Quantal phase factors accompanying adiabatic changes, Proc. R. Soc. A **392**, 45 (1984).

[50] V. Kantsler and R. E. Goldstein, Fluctuations, Dynamics, and the Stretch-Coil Transition of Single Actin Filaments in Extensional Flows, Phys. Rev. Lett. **108**, 038103 (2012).

[51] See Supplemental Material at http://link.aps.org/supplemental/10.1103/PhysRevLett.130.258402 for further description of the mode representation, constrained linear models, and model inference procedure.

[52] J. P. Boyd, *Chebyshev and Fourier Spectral Methods* (Courier Corporation, New York, 2001).

[53] J. N. Kutz, S. L. Brunton, B. W. Brunton, and J. L. Proctor, *Dynamic Mode Decomposition: Data-Driven Modeling of Complex Systems* (SIAM, Philadelphia, 2016).

[54] P. J. Baddoo, B. Herrmann, B. J. McKeon, J. N. Kutz, and S. L. Brunton, Physics-informed dynamic mode decomposition (piDMD), arXiv:2112.04307.

[55] D. P. Kingma and J. Ba, Adam: A method for stochastic optimization, arXiv:1412.6980.

[56] S. Wright and J. Nocedal, *Numerical optimization*, Springer Series in Operations Research and Financial Engineering (Springer, New York, 1999).

[57] J. Zhuang, T. Tang, Y. Ding, S. C. Tatikonda, N. Dvornek, X. Papademetris, and J. Duncan, Adabelief optimizer: Adapting stepsizes by the belief in observed gradients, Adv. Neural Inf. Process. Syst. **33**, 18795 (2020).

[58] S. L. Brunton, J. L. Proctor, and J. N. Kutz, Discovering governing equations from data by sparse identification of nonlinear dynamical systems, Proc. Natl. Acad. Sci. U.S.A. **113**, 3932 (2016).

[59] K. Ye and L.-H. Lim, Schubert varieties and distances between subspaces of different dimensions, SIAM J. Matrix Anal. Appl. **37**, 1176 (2016).

[60] J. M. Gray, J. J. Hill, and C. I. Bargmann, A circuit for navigation in Caenorhabditis elegans, Proc. Natl. Acad. Sci. U.S.A **102**, 3184 (2005).

[61] R. E. Goldstein and D. M. Petrich, Solitons, Euler's Equation, and Vortex Patch Dynamics, Phys. Rev. Lett. **69**, 555 (1992).

[62] H. Hasimoto, A soliton on a vortex filament, J. Fluid Mech. **51**, 477 (1972).